Journal of Applied Polymer Science

Investigation of Thermal, Rheological, and Physical Properties of Amorphous Poly(ethylene terephthalate)/Organoclay Nanocomposite Films

Tolga Gökkurt,[1] Ali Durmus,[2] Vedat Sariboga,[2] M. A. Faruk Öksüzömer[2]

[1]Faculty of Technology, Department of Metallurgical and Materials Engineering, Sakarya University, Serdivan, Sakarya 54187, Turkey

[2]Engineering Faculty, Department of Chemical Engineering, Istanbul University, Avcılar, Istanbul 34320, Turkey

Correspondence to: A. Durmus (E-mail: durmus@istanbul.edu.tr)

ABSTRACT: Thermal, rheological, and physical properties of amorphous poly(ethylene terephthalate) (PET)/organoclay nanocomposite films which were successfully prepared with melt processing method using a PET/organoclay masterbatch were studied in detail. Structural and physical properties of the films were characterized by the UV–Vis spectroscopy, XRD and SEM analysis, DSC, DMA, and rheological tests and gas permeability measurements. Cold-crystallization behavior of the samples was analyzed by the DSC and DMA methods. Aspect ratio of the organoclay layers were determined with the Nielsen and Halpin-Tsai models based on the gas permeability and DMA data, respectively. It was found that the organoclay reduced the nonisothermal cold-crystallization rate of PET chains by restricting the segmental motion of the polymer in the solid state. On the other hand, the organoclay enhanced the nonisothermal melt-crystallization of PET due to the nucleation effect. Aspect ratio (A_f) of the clay layers were found to be about 20 by using the gas permeability and DMA data. Aspect ratio value was also confirmed by the analysis of SEM images of the samples. A physical model for the sample microstructure was offered that the stacks with the thickness of 20–30 nm and the lateral size of 400–600 nm, probably consisting of 5–8 layers, were uniformly dispersed in the PET structure. © 2013 Wiley Periodicals, Inc. J. Appl. Polym. Sci. 129: 2490–2501, 2013

KEYWORDS: polyesters; clay; structure–property relations; packaging

Received 30 October 2012; accepted 9 December 2012; published online 30 January 2013

DOI: 10.1002/app.38982

INTRODUCTION

Poly(ethylene terephthalate) (PET), the most widely used and low-cost member of thermoplastic polyesters, has wide variety of applications such as fibers, packaging films, food and beverage bottles, and parts in automotives and electronics due to its superior thermal and mechanical properties, low permeability, and chemical resistance. In recent years, a growing market and an emerging technology demands have been reported for the beverage applications of PET, especially for beer, as a rigid packaging material.[1] Providing high impermeability and transparency are the most important properties of such materials for the packaging applications. Structural or chemical modifications and physical compounding routes are two main approaches to improve gas barrier performance of PET.

Hu et al.[2] studied the physical properties of PET random and blocky copolymers with isophthalate units. They developed a structural model for the oxygen transport throughout the PET copolymers including various isophthalate units, 10%, 20%, and 30%. They showed that the comonomer distribution strongly affects the crystallization behavior of PET and thus significantly affects the oxygen permeability. In their study, it has been shown that the blocky copolymers crystallized more rapidly than PET, due to the enhanced spherulite nucleation. They also concluded that the interlamellar amorphous regions of PET exhibited lower density than that of the amorphous matrix as a result of the constrained nature of amorphous chain segments attached to crystallites while the copolymers including isophthalate units prevents de-densification of the interlamellar amorphous regions.

On the other hand, compounding of PET with higher barrier components such as ethylene vinyl alcohol copolymers (EVOH), liquid crystalline polymers (LCP), and aromatic polyamides and/or composite approach are more convenient methods to improve gas permeability of PET, for the industrial applications. Hu et al.[3] studied gas barrier properties of PET blended with an aromatic polyamide, either poly(*m*-xylene adipamide) (MXD6)

or a copolyamide, based on MXD6 in which 12 mol % adipamide was replaced with isophthalamide (MXD6-12I). They reported that formation of platelets from the less permeable aromatic polyamide domains by stretching effectively reduced the gas permeability of blends. Polyakova et al.[4] investigated the effect of cold-crystallization from the glassy state on the oxygen-barrier properties of copolyesters based on ethylene terephthalate with up to 10 mol % of isophthalate, phthalate, or naphthalate. They found that three comonomers showed similar effect to significantly decrease the oxygen permeability of PET although the comonomers affected differently the chain configuration. Polyakova et al. concluded that introduction of small amounts of comonomer can alter the chain configuration, and thus chain packing, in the amorphous phase. It has also been speculated that such constrained configurational freedom restricted segmental relaxation during cold crystallization and made possible permanent packing defects.

In recent years, a considerable research effort has been conducted for the development of PET/clay nanocomposites to improve the gas barrier performance of PET that is essentially required for beverages bottles and packaging films. Aht-Ong and Benjapornthavee[5] studied the preparation of PET/montmorillonite nanocomposite films by solution mixing and casting techniques. They reported that highly transparent PET/montmorillonite and PET/organo-montmorillonite films with the enhanced mechanical properties were successfully prepared by solution blending under the ultrasonic power. But only few studies have been reported on the physical properties of PET/clay nanocomposite films due to the processing difficulties. Recently, Ghasemi et al.[6] reported a detailed discussion on the physical properties of PET/clay nanocomposites prepared via melt compounding by using various organoclays. They also studied on the effects of processing conditions on properties of PET/clay nanocomposite films.[7] Even in the PET/organoclay nanocomposites, some authors used various polymeric components as compatibilizer similar to the nonpolar polymers such as polyethylene and polypropylene. Vidotti et al.[8] prepared PET/organo-montmorillonite nanocomposites via melt compounding method in a twin screw extruder and studied the effects of using a polyester ionomer as a compatibilizer on the properties of PET/organo-montmorillonite nanocomposites. They reported that the PET-based ionomer efficiently promoted the intercalation/exfoliation of the organo-montmorillonite in the PET matrix.

Choi et al.[9] prepared PET/clay nanocomposite by the direct polymerization with clay-supported catalyst. They reported that the microstructure of samples including 1, 3, and 5% of clay were intercalated. But highly transparent films were successfully obtained and the gas permeability performance of the nanocomposite films significantly improved compared to PET, in their study.

On the other hand, many studies have been published about the preparation and characterization of PET nanocomposites prepared with various types of nanofillers such as layered double hydroxides,[10] silica,[11] alumina,[12,13] barite,[14] polyhedral oligomeric silsesquioxanes (POSS),[15] and carbon-based nanomaterials (nanotubes, graphites, etc.)[16–20] by melt processing methods. Studies, reported so far, on the PET/clay or PET/organoclay nanocomposites have mainly focused on the crystallization behavior and kinetics rather than a comprehensive investigation of the physical properties of these materials.[21–25]

In this study, amorphous and highly transparent PET/organoclay nanocomposite films were successfully prepared by melt blending and film casting methods using a PET/organoclay masterbatch which was prepared in a twin screw extruder. Thermal and physical properties of amorphous PET/organoclay nanocomposite films were investigated in detail.

EXPERIMENTAL

Materials

The PET resin used in this study was MELPET® 760 [intrinsic viscosity, IV, of 0.76 ± 0.02 dL/g (ASTM D4603), density of 1.40 ± 0.01 g/cm^3 (ASTM D1505) and carboxylic end group content of 20 ± 10 eq./ton (titration method)], obtained from Meltem Kimya, TR. The clay employed in this study was a commercial grade organoclay, Nanomer® I.30E which is an onium ion, octadecylamine, surface-modified montmorillonite mineral, supplied from Nanocor. Organic group content of the Nanomer® I.30E was declared as 25–30 wt % by the manufacturer.

Melt Processing and Film Extrusion

Before melt processing, PET and organoclay were dried in a vacuum oven overnight at 105°C. The PET/org-clay nanocomposite films were prepared via masterbatch dilution method by melt processing in two steps. In the first step, a masterbatch including 20 wt % of organoclay, Nanomer® I.30E, was prepared in a lab scale co-rotating twin screw extruder (Werner&Pfleider GmbH. ZSK 25) with a screw speed of 300 rpm. Screw diameter (D) and L/D value of the twin screw extruder are 25 mm and 48, respectively. A temperature profile of 235-240-245-250-250-260°C was applied throughout the barrel from the feeding zone to die.

In the second step, the masterbatch was diluted in a single screw extruder with a screw speed of 50 rpm to prepare (Labtech Engineering Scientific, D: 20 mm and L/D: 30) nanocomposite films by using a slit die and cast film haul-off unit. A temperature profile ranged between 240 and 265°C was applied throughout the barrel from the feeding zone to die. Draw out speed in the haul-off unit was applied as 2.5 m min^{-1}. The film thicknesses ranged between 100 and 120 μm.

Final compositions of the films are given in Table I. Volume fraction of the filler, Nanomer® I.30E organo-clay, (ϕ_f) was calculated according to the following formula:

$$\phi_f = \frac{\rho_p W_f}{\rho_f W_p + \rho_p W_f} \quad (1)$$

where ρ_p and ρ_f are the densities and W_p and W_f are the weight fractions of the PET and organoclay, respectively. The density value of Nanomer® I.30E was taken as 1.71 g cm^{-3}.

Microstructural and Physical Characterization of the Samples

The transparency of PET and nanocomposite films was monitored by measuring the light transmittance (T%) between the

Table I. Sample Compositions

Samples	wt (%) PET	wt (%) org-clay	Volume fraction of the filler (ϕ_f)
PET	100	0	0
I.30-1	99	1	0.0082
I.30-3	97	3	0.0247
I.30-5	95	5	0.0413

wavelength of 190–1100 nm in a PerkinElmer Lambda 35 series UV–Visible spectroscopy with an integrating sphere accessory.

XRD analysis of the film samples were performed with a Rigaku D/Max-2200/PC model wide angle X-ray Diffractometer (XRD) with a Cu Kα, running at 40 kV and 40 mA, scanning from 2° to 35° with the step of 0.1° at room temperature. Intergallery distance between clay layers in nanocomposites was calculated by the Bragg's equation:

$$n\lambda = 2\mathrm{d}\,\mathrm{Sin}\,\theta \tag{2}$$

where n is an integer determined by the order given ($n = 1$), d is the spacing between clay layers, λ is the wavelength of X-ray equal to 0.154 nm, and θ is the angle of diffraction.

Sample morphology was investigated by a field emission scanning electron microscope (FE-SEM, FEI Quanta FEG 450) operated at 30 kV. Cryo-fractured surfaces of the film samples were directly imaged in the electron microscope after a proper sample preparation of sputter-coated with gold.

Melting and crystallization behavior of the samples were carried out in a heat flux type DSC, SII Nanotechnology ExStar 6200. Temperature and heat flow calibration of the instrument were achieved with high purity indium (In), tin (Sn), and zinc (Zn) metals. In nonisothermal crystallization runs, samples weighing about 9–10 mg in an aluminum crucible were heated from 0°C to 280°C with the heating rate of 5°C min^{-1} and kept at this temperature for 2 min to remove the thermal history then cooled from 280°C to 0°C with the cooling rate of 5°C min^{-1} by an electrical cooling device, Thermo Scientific EK90C/SII intracooler. After completion of the melt-crystallization process, samples were kept at 0°C for 2 min. Subsequently, nonisothermally crystallized samples were heated again from the 0°C to 280°C with the heating rate of 10°C min^{-1}. Degree of crystallinity (X_c) were determined from the second melting enthalpy values using the following equation:

$$\mathrm{X_c}(\%) = \frac{\Delta \mathrm{H}_m}{(1-\alpha)\Delta \mathrm{H}_m^{\mathrm{o}}} \times 100 \tag{3}$$

where ΔH_m is second melting enthalpy of the samples (J g^{-1}), ΔH_m^o is the enthalpy value of melting of a 100% crystalline form of PET (140 J g^{-1}),[26] and α is the total weight fraction of fillers and additives. All runs were carried out under nitrogen (N_2) atmosphere at a flow rate of 50 mL min^{-1} to prevent thermal degradation of the samples.

Viscoelastic behavior of the samples was analyzed by a dynamic oscillatory rheometer in the melt state. A controlled strain rheometer (AR-G2, TA Instruments) equipped with 25 mm diameter parallel plate geometry was employed for the rheology tests. Samples were directly loaded and molded between the plates and rheological tests were carried out at 260°C with a gap distance of 1 mm under nitrogen atmosphere. First, strain sweep test was performed from the initial strain value of 0.1 to a final strain value of 50 in percent, with the angular frequency of 1 rad s^{-1} to determine the linear viscolelastic (LVE) region of the samples. Storage (G') and loss (G'') modulus of the samples were recorded as a function of shear strain (γ%). In the frequency sweep tests, a small amplitude oscillatory shear was applied to the samples. The G', G'', and dynamic viscosity (η^*) were measured as a function of angular frequency (ω) in the range of 0.1–100 rad s^{-1} at a strain value in the LVE region (strain magnitude of 0.01).

Oxygen permeability tests were performed with a permeability testing apparatus, GDP C-2000 (Brugger Feinmechanik GmBH) working according to manometric method, (ASTM 1434) at 25°C and 50% relative humidity. Thicknesses of the test specimens, which were measured with a micrometer at 10 points at least, were within ±5%. Samples were masked by an aluminum foil for exposing the permeation area of 22.9 cm^2. O_2 gas (purity of 99.9%) used in the permeation measurements was obtained from a commercial supplier. For each sample, three different films were tested and the average permeability (P) values are reported with the standard deviations, as normalized for the film thickness of 100 μm.

Dynamic mechanical analysis of the film samples obtained from the cast film unit was performed with a DMA (ExStar 6100, SII Nanotechnology). The height and width of the test specimens were 20 and 10 mm, respectively. The DMA test was performed in tension mode at a frequency of 1.0 Hz, a strain amplitude of 10 μm, and the temperature range of 20–300°C with the heating rate of 2°C min^{-1}.

RESULTS AND DISCUSSION

Film Transparency by UV–Vis Spectroscopy and Microstructure by XRD and SEM

Photographs of the PET/organoclay masterbatch used in the study and nanocomposite films including various amounts of organoclay, Nanomer® I.30E, are seen in Figure 1. It could be clearly seen that the PET and nanocomposite films are optically transparent. In film or packaging applications, transparency of nanocomposites is considered to be the most important visual quality and aesthetic factor. In most cases, melt blended nanocomposite films are highly opaque and their appearance turns yellowish or light-brownish color even though they provide superior physical performances. There might be several reasons originated from the structural features of materials and processing history for hazy film formation. Structural phenomena are commonly poor dispersion of clay layers and/or thermal degradation issues. If the clay layers cannot be dispersed in nanoscale, large stacks or particles usually scatter the light and thus reduce the light transmittance and the optical clarity of films. On the other hand, transparency of polymer/clay nanocomposite films

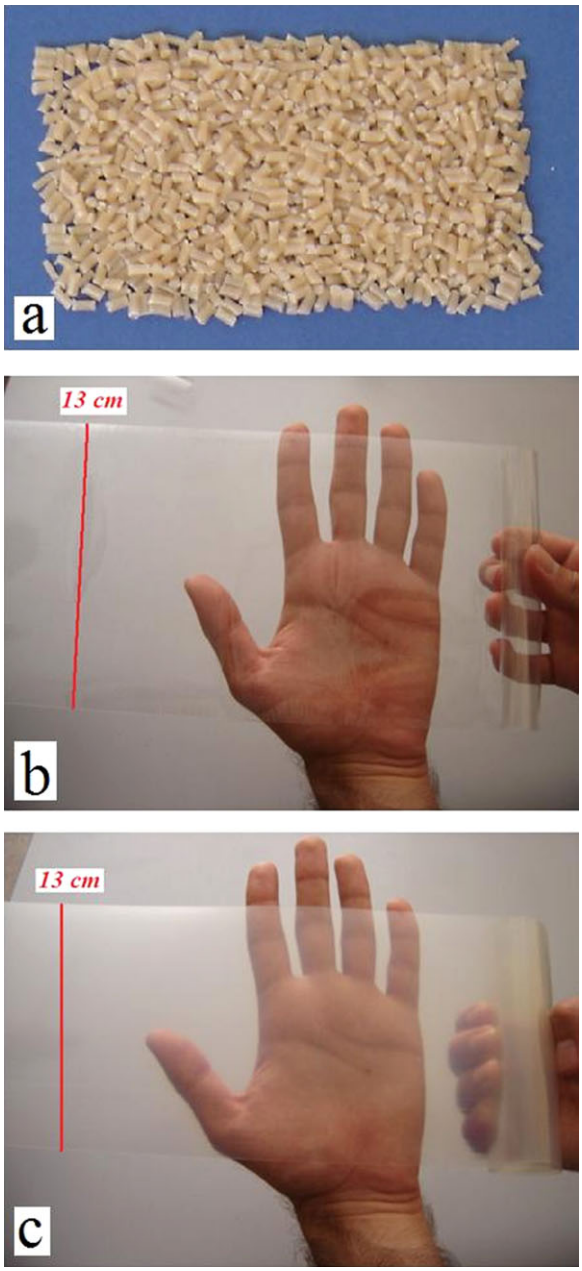

Figure 1. Photographs of the masterbatch and nanocomposite films. (a) PET/organoclay masterbatch, (b) PET film, and (c) I.30-3 film. [Color figure can be viewed in the online issue, which is available at wileyonlinelibrary.com.]

is depended on the crystallite size of polymer which is related to the nucleation effect of clay layers resulting in the formation of smaller crystals than the wavelength of visible light and allowing light pass-through without any scattering, cooling and stretching conditions, etc.

In the present study, it is concluded that the nanocomposite films, especially including 1 wt % and 3 wt % of organoclay promise sufficient transparency for commercial applications. But, the film sample of I.30-5 was hazy, an unacceptable property for film applications.

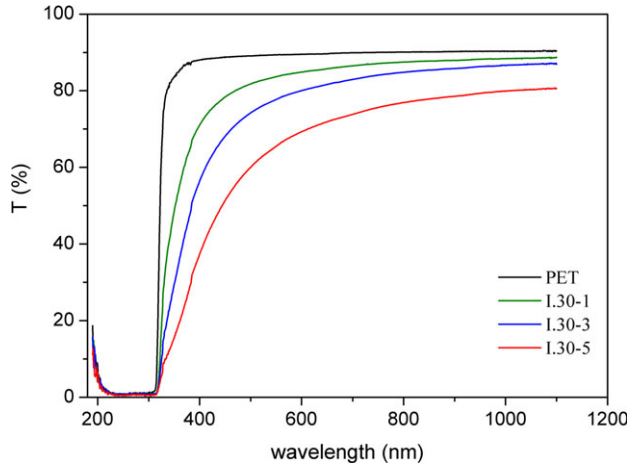

Figure 2. UV–Vis transmittance spectrum of the samples. [Color figure can be viewed in the online issue, which is available at wileyonlinelibrary.com.]

The transparency of the films was also studied by measuring the light transmittance (T%) in the visible light region. The UV–Vis transmission spectra of films are given in Figure 2. It is seen that the PET film is highly transparent in the visible region (T%: 90.3 in the wavelength between 390 and 1100 nm). In the visible region, the T% values reduced with the increasing of organoclay amount in the PET/organoclay nanocomposite samples, as expected.

Another result is that the T% gradually increases with the increasing of wavelength in the visible region for the nanocomposite films depending on the amount of organoclay while it is constantly 90% in that range of wavelength for the PET film. This is due to the presence of large clay stacks and their light scattering effect. At the wavelength of 1000 nm, the T% values of PET, I.30-1, I.30-3, and I.30-5 samples are 90.3, 88.4, 86.6, and 80.0, respectively. It should be noted that the decreasing of transparency due to the presence of large clay stacks and particles and the increase in transparency resulted from the reduced spherulite size could compensate the each other. Thus, isothermal and nonisothermal cold- and melt-crystallization kinetics and the physical properties of films related to the crystalline structure will be reported in detail in another manuscript.

X-ray diffraction (XRD) patterns of the organoclay, Nanomer® I.30E, and film samples are given in Figure 3. Characteristic diffraction peaks for the organoclay were observed at the diffraction angle (2θ) of 4.14 and 8.06. Corresponding intergallery distance between the organoclay layers (d_{001}) was determined as 2.14 nm by using the Bragg equation. In the nanocomposite film sample including 1 wt % of organoclay, no peak was observed. This observation is generally attributed to the exfoliated structure. But, it might be due to the presence of less organoclay in the sample than the detection limit of the analysis. On the other hand, d_{001} peak is also clearly seen, but shifted to lower diffraction angles in the I.30-3 and I.30-5 samples. This result is more pronounced for the I.30-5 sample. Shifted and visible peaks suggest that intergallery distance is increased but relatively large stacks of clay platelets are still present in the

Applied Polymer SCIENCE

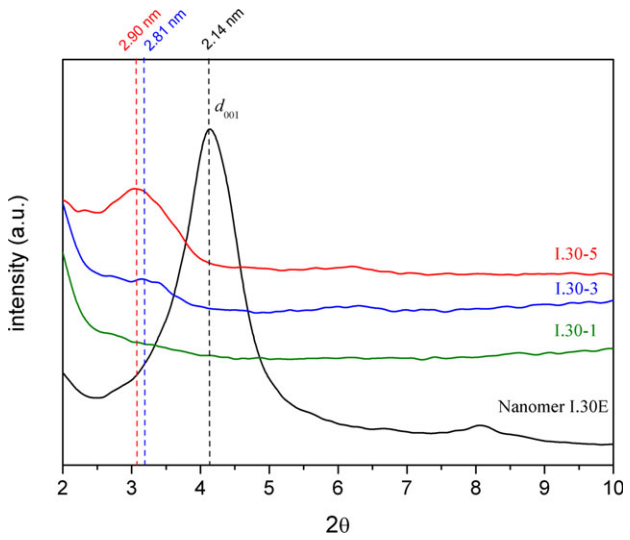

Figure 3. XRD patterns of the organoclay and PET/organoclay nanocomposite films. [Color figure can be viewed in the online issue, which is available at wileyonlinelibrary.com.]

I.30-5 sample showing clay layers being not completely exfoliated. Intergallery distance was calculated 2.81 nm for the I.30-3 and 2.90 nm for the I.30-5 by using the Bragg equation. Based on the XRD results, the I.30-1, I.30-3, and I.30-5 samples can be designated as exfoliated, semi-exfoliated, and intercalated, respectively.

SEM images of the fractured surfaces of the films are given in Figure 4. As seen in Figure 4(a,b), the fractured surface of PET film is quite smooth which indicates a typical brittle failure. It is clearly seen that the fractured surfaces of PET/organoclay nanocomposite films particularly display roughness and many sharp-edged sheets which can be attributed to the dispersed organoclay layers and stacks. This coarsening becomes more intense in a unit volume of sample when the amount of organoclay increases. At this magnification given in Figure 4, it is difficult to distinguish the lateral size of clay stacks. The detailed SEM images of I.30-5 sample taken at higher magnification are given in Figure 5. Figure 5(a) shows the top view of a group of clay-stacks embedded into the PET structure. It can be seen that the average width of stacks are about 400–600 nm. Figure 5(b) shows the side view of a clay stack embedded into the polymer phase. The stack thickness is estimated to be 20–30 nm. By obtaining the lateral size and thickness of the clay layers or stacks, average aspect ratio of the filler can be estimated. Aspect ratio (A_f) is known as the ratio of width to thickness of the filler (l/d) which is an indicative parameter for filler dispersion in composite systems. In polymer-clay nanocomposites, aspect ratio is the highest for completely exfoliated structures depending on the lateral size of the clay layers. The average aspect ratio of organoclay stacks is about 20 by the analysis of SEM images. This value is based on the direct observation of morphology and microstructure of the samples. In the following parts, the A_f will also be calculated by several mathematical approaches taking into account of the physical properties of samples.

Crystallization and Melting Behavior of the Film Samples

Crystallization and melting curves of the samples are given in Figure 6. Figure 6(a) shows the DSC thermograms of the amorphous film samples recorded during the first melting. The glass transitions (T_g) and cold-crystallization peaks of the samples are seen in this figure. First melting endotherms of the samples are not given here since a significant difference is not observed depending on the sample composition. The melt-crystallization exotherms and subsequent second melting endotherms of the samples are also given in Figure 6(b,c), respectively. The crystallization and melting parameters of samples are listed in Table II.

It was found that introducing organoclay increased the cold-crystallization onset and peak temperatures of PET, except the I.30-1 sample. This increase is due to the restriction effect of clay layers or stacks on the mobility of PET chains above the glass transition temperature (T_g). This effect is obviously seen by comparing the peak half-width values of the crystallization exotherms ($w_{1/2}$) which defined as the width of the peak at its half height and schematized in Figure 6(b). It can be used to simply compare the overall crystallization rate of various samples during heating or cooling. The parameter $w_{1/2}$ is also dependent on the crystal size distribution. By comparing the $w_{1/2}$ values given in Table II, it can be clearly seen that the PET/organoclay samples exhibited higher $w_{1/2}$ values than PET which implied that the nanocomposites needs more time to complete cold-crystallization process. It is well known that the conformational arrangement of polymer chains from glassy to crystalline state is based entirely on the molecular reptation in cold crystallization. Therefore, cold-crystallization of polymers often requires a certain amount of energy to overcome the potential barrier to segmental motion, whereas the melt crystallization is driven by undercooling. Introducing an inorganic filler into the PET physically restricted the chain mobility and increased the energy barrier for the segmental motion. On the other hand, the enthalpy of crystallization (ΔH_c) for the cold-crystallization process reduced with the increasing amount of organoclay.

But, in the melt-crystallization process, organoclay addition exhibited reverse effects on the crystallization compared to the cold crystallization. Crystallization onset ($T_{c\text{-}o}$) and peak ($T_{c\text{-}p}$) temperature of the I.30-1 sample did not significantly differ from those of PET. But, addition of higher amount of organoclay considerably shifted the $T_{c\text{-}p}$ value to higher temperatures. This result points out that organoclay acts as nucleating agent in the melt crystallization and possibly increase the melt-crystallization rate of PET. Similar relationship has been reported before for the isothermal or nonisothermal melt-crystallization behavior of PET[14] and other thermoplastic polyesters[27–30] based nanocomposites. The enthalpy of crystallization (ΔH_c) for the melt-crystallization process also reduced with the increasing amount of organoclay.

Second melting endotherms of the samples crystallized at a relatively slow cooling rate (5°C min^{-1}) show double melting peaks which signify formation of different crystallite sizes. The low temperature secondary peak varied in the range of 243.0–244.2°C while the high temperature main peak differed in

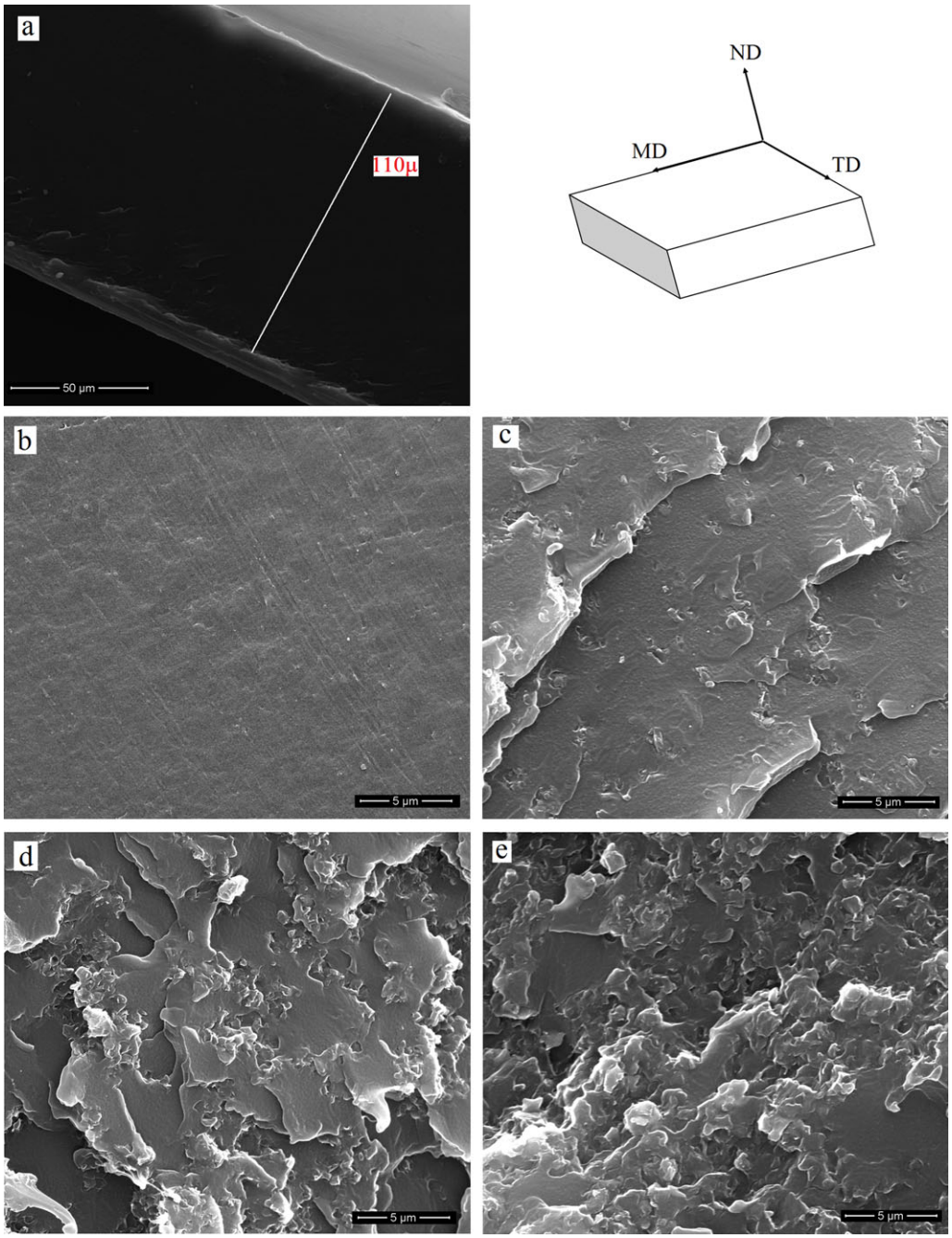

Figure 4. SEM images taken from the cryo-fractured cross-sections of the films (×10,000). (a and b) PET, (c) I.30-1, (d) I.30-3, and (e) I.30-5. MD, machine direction; TD, transverse direction; ND, normal direction. [Color figure can be viewed in the online issue, which is available at wileyonlinelibrary.com.]

between 249.0 and 250.3 depending on the sample composition. As seen, second melting peak temperatures ($T_{m\text{-}p\ I}$ and $T_{m\text{-}p\ II}$) were not affected much by the sample composition. Double melting endotherms could attribute to the different spherulite sizes and crystal perfection depending on the recrystallization issues during the second heating run. But, it was found that the values of second melting enthalpy and corresponding degree of crystallinity (X_c%) values decreased with the increasing of organoclay amount. This is probably due to the adverse effect of organic groups onto the clay layers on the crystallization of PET. We previously reported that the organic ammonium groups in the organoclays decelerate the crystallization rate of thermoplastic polyesters by possibly affecting the rate of chain transfer to growing crystal face and folding.[22,31] To comprehensively understand the effects of organoclay on the cold- and melt-crystallization of amorphous PET/organoclay samples, analysis of

Applied Polymer SCIENCE

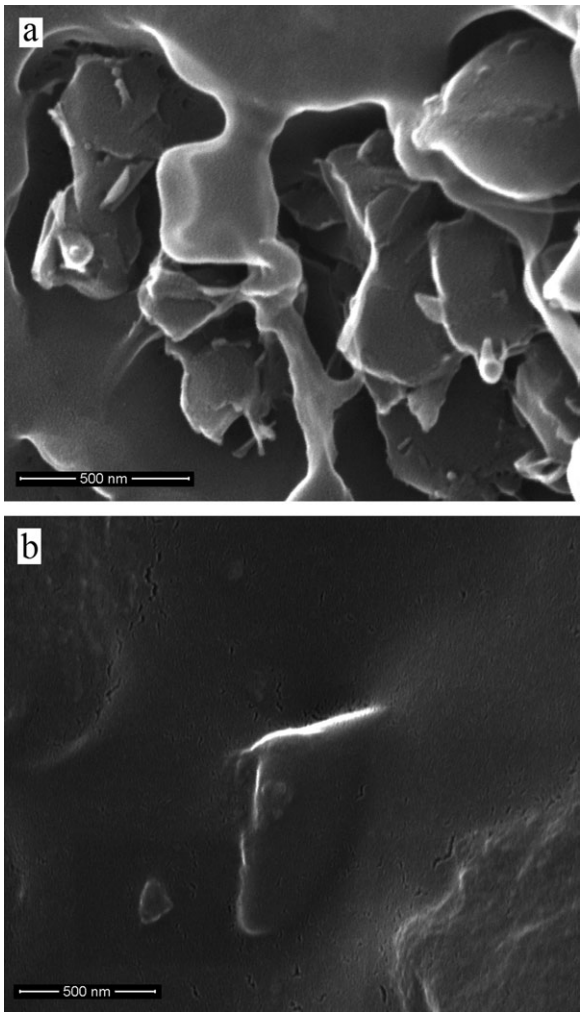

Figure 5. SEM images of the I.30-5 sample at higher magnifications. (a) ×150,000 and (b) ×120,000.

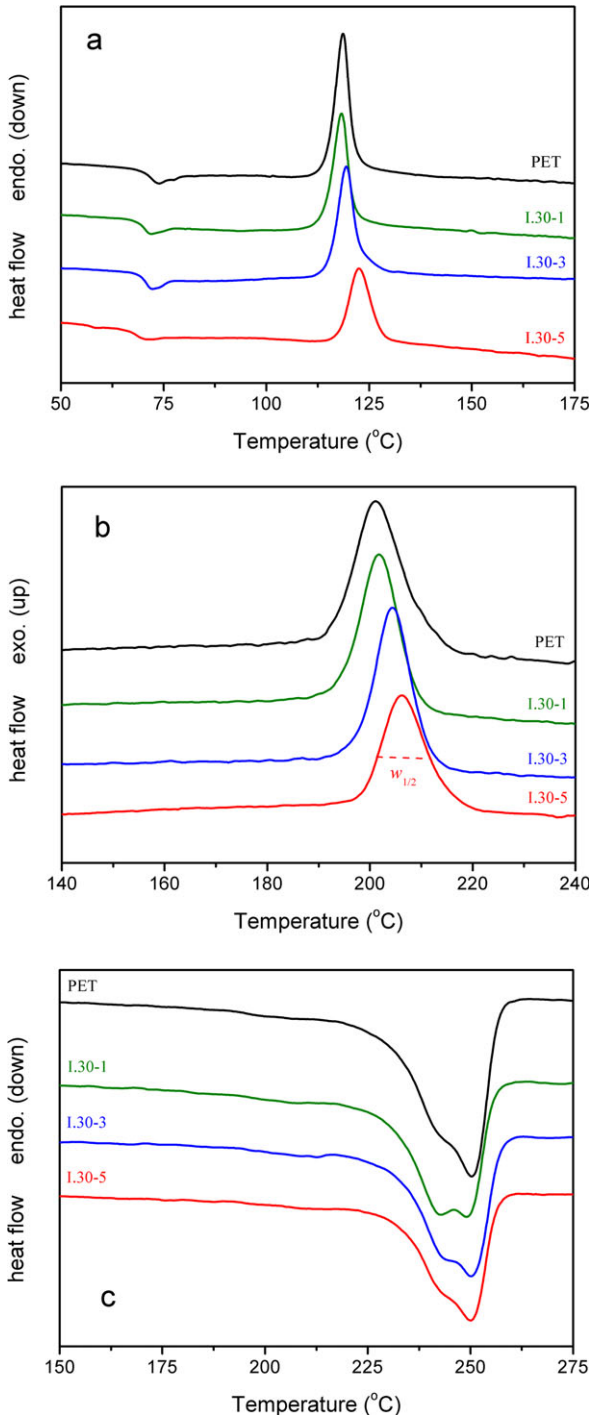

Figure 6. DSC thermograms of the PET and PET/organoclay nanocomposite films. (a) First melting, (b) cooling, and (c) second melting runs. [Color figure can be viewed in the online issue, which is available at wileyonlinelibrary.com.]

crystallization behavior, microstructure formation, and cold- and melt-crystallization kinetics of the samples will be reported in a separate manuscript, in detail, depending on the sample composition.

Rheological Behavior of the Samples

Rheological behavior of polymer composites in the melt state is very critical to understand processability and structure–property relationships of such materials. On the other hand, melt rheology measurements can probe the behavior of relatively large material that is crucial from the macroscopic point of view. Melt rheology tests are rapid, easy, and precise tools for evaluating the filler dispersion and interfacial interactions in polymer composites.

In rheology tests, first dynamic strain sweep test was applied to samples in order to characterize strain dependence of the viscoelastic properties of the samples and determine linear viscoelastic (LVE) region. Since the storage modulus (G') is a more sensitive rheological function than the loss modulus (G'') to the structural changes of the composites, only the storage modulus curves are presented in this study. Dependence of storage modulus on the shear strain is given in Figure 7(a) for the PET and PET/organoclay nanocomposites. For polymer melts, storage

Table II. Crystallization and Melting Parameters of the Samples

	Cold crystallization				Melt crystallization				Second melting			
Samples	$T_{c\text{-}o}$ (°C)	$T_{c\text{-}p}$ (°C)	$w_{1/2}$	ΔH_c (J g^{-1})	$T_{c\text{-}o}$ (°C)	$T_{c\text{-}p}$ (°C)	$w_{1/2}$	ΔH_c (J g^{-1})	$T_{m\text{-}p\ I}$ (°C)	$T_{m\text{-}p\ II}$ (°C)	ΔH_m (J g^{-1})	X_c (%)
PET	114.2	118.6	3.8	35.0	212.0	201.0	10.8	53.1	243.6	250.2	44.1	31.5
I.30-1	113.7	118.3	4.2	25.3	209.7	201.8	8.7	41.0	242.9	249.2	33.8	24.4
I.30-3	114.7	119.5	4.8	23.9	212.0	204.4	8.0	37.8	244.2	250.3	30.4	22.4
I.30-5	117.6	122.6	6.0	23.2	215.8	206.2	9.6	35.0	243.2	250.1	28.5	21.4

modulus exhibits a linear region (Newtonian plateau) at low strains and deviate from this linearity by generally reducing in G' at high strain amplitudes. This deviation is called the Newtonian to non-Newtonian transition in which the strain value around the deviation is defined as the critical strain (γ_c). Amplitude of the plateau modulus is a critical parameter to qualify enhancement effect of the fillers on the physical properties of composite materials. As seen in Figure 7(a), the nanocomposite samples exhibit higher G' values than PET in entire range of strain and this enhancement in G' increases gradually with the increasing of organoclay amount. In this study, PET and I.30-1 samples displayed Newtonian behavior at the entire strain range studied. But, the I.30-3 and I.30-5 samples showed transition region at higher strains. As seen in Figure 7(a), the critical strain values are about 30% and 3% for the I.30-3 and I.30-5 samples, respectively. Lower critical strain values represent that the rheological behavior of the sample is more sensitive to shear strain than those of other samples.

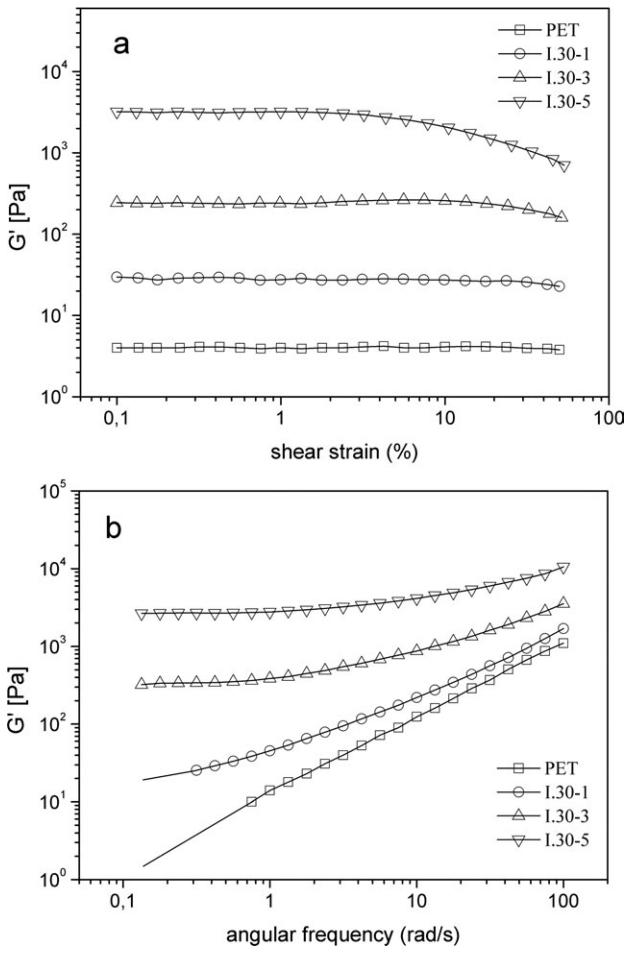

Figure 7. Rheological behavior of the samples. (a) Dependence of storage modulus (G') on the shear strain (γ%) and (b) dependence of the storage modulus (G') on the angular frequency (ω, rad/s).

Figure 7(b) shows the frequency dependence of G' of the PET and PET/organoclay nanocomposites obtained from the frequency sweep test. PET/organoclay samples showed higher storage modulus values than the PET in entire frequency region. For linear polymers, dependence of G' and G'' on the frequency is expected to be ω^2 and ω^1, respectively, in the melt state. But large deviations could occur for the cross-linked systems or network structures. In this study, the PET resin exhibited lower scaling value, ~0.95 at terminal (or low frequency) region. Similar behavior reported by Hu et al.[32] for the rheological behavior of PET resin ($G' \propto \omega^{1.2}$ and $G'' \propto \omega^{0.9}$).

It is also known that frequency dependence of G' at low frequency region is the critical assessment for the microstructural features of composite materials.[33,34] At low frequency region, it was observed that G' for the both composite samples becomes frequency independent ($G' \propto \omega^0$) which is characteristic behavior of solid-like materials. Magnitude of low frequency improvement in G' indicates dispersion level of filler and/or interfacial interactions between the filler and polymer matrix. This interaction depends on the various structural and physical parameters such as amount and effective surface area of filler, level of

Table III. Oxygen Permeability Values of the Films

Samples	P (cc. 100 μ/m^2 day atm)
PET	70.0 ± 3.1
I.30-1	65.3 ± 2.2
I.30-3	54.0 ± 3.7
I.30-5	45.7 ± 5.5

Applied Polymer SCIENCE

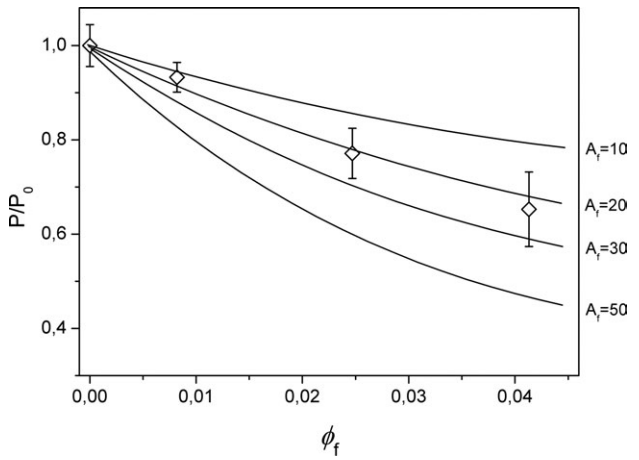

Figure 8. Nielsen model applied to gas permeability data of the samples for estimating the aspect ratio of clay layers.

dispersion, filler geometry, processing methods, and amount of functional group in the system. It is clearly seen in the Figure 7(b) that the nanocomposite samples showed higher G' in entire frequency region and became frequency independent at low frequencies.

Oxygen Permeability

High barrier and transparent polymer/clay nanocomposite packaging films are considered one of the novel innovations in barrier technologies.[35] Oxygen (O_2) permeability (P) values of the film samples are listed in Table III. It is seen that the addition of 5 wt % of org-clay reduced the P value of PET about 35%.

One might consider that improvement in the gas barrier performance of PET/organoclay films could be related to the degree of crystallinity value. But, the specimens used in this study for the gas permeability tests were amorphous and transparent films. No peak was observed in the XRD patterns of the PET and nanocomposite films between the diffraction angle of 15°-35° which corresponds to polymer crystals (not given here). Therefore, it is obviously inferred that the improvement in barrier performance of the films only originated from the amount of filler and level of dispersion and thus the tortuosity approach can be applied to the permeability data. Furthermore, it should be noted that the introducing of organoclay reduced the degree of crystallinity of PET by taking into account the heat of fusion and degree of crystallinity values given in Table II.

One of the most widely used approaches for quantitatively predicting the decrease in permeability of a diffusing molecule in a polymer containing impermeable fillers is the Nielsen model.[36] The Nielsen model assumes that two-dimensional diffusion occurs through a polymer containing infinitely long, rectangular cross-section plates that were uniformly dispersed in the matrix but were placed normal to the direction of gas transfer path. Because a diffusing gas molecule cannot permeate the clay platelets, it must go around them thus leading to a tortuous path.

Nielsen model defined as:

$$\frac{P}{P_0} = \frac{1-\phi}{1+A_f/2\phi} \tag{4}$$

where P is the permeability value of composite, P_0 is the permeability value of polymer, ϕ is the volume fraction of filler, and A_f is the aspect ratio of filler. Model parameters are only the amount of filler and degree of dispersion. It can be clearly predicted from the equation that the relative permeability (P/P_0) decreases with the increasing of aspect ratio (degree of exfoliation) and concentration of the clay. Relationship between the relative permeability and volume fraction of organoclay is given in Figure 8. By applying the Nielsen model to the experimental oxygen permeability data, the aspect ratio was found to be ~20. This estimation is very consistent with that obtained from the SEM images.

Mechanical Properties of the Films

Changes in the storage modulus (E') and loss factor (Tan δ) of the PET and PET/organoclay nanocomposite films as a function

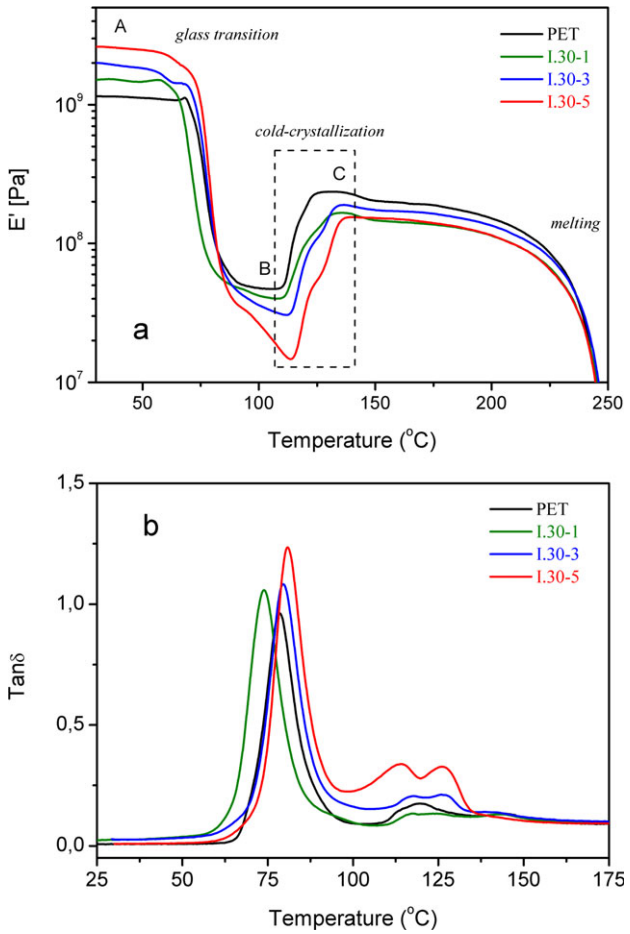

Figure 9. DMA curves of the films. Dependence of (a) storage modulus (E') and (b) loss factor (tan δ) on the temperature. [Color figure can be viewed in the online issue, which is available at wileyonlinelibrary.com.]

of temperature are given in Figure 9(a,b), respectively. It is well known that DMA is a widely used and rapid tool for precisely probing relaxation issues in polymers, blends and composites and characterization of their viscoelastic properties in solid state. All the thermal transitions and mechanical behavior of samples are seen in the storage modulus curves given in Figure 9(a). The storage modulus curves of the samples display three distinctive regions depending on the temperature. These regions represent the glassy plateau (A), rubbery region before (B) and after (C) the cold-crystallization. As expected, the storage modulus of the nanocomposite samples below glass transition (at A) increases substantially with the amount of organoclay due to the stiffening effect of clay layers which also implies efficient stress transfer between the PET and filler phases. In the glass transition region, the storage modulus significantly reduced followed by an increase up to a second plateau due to the cold crystallization. Following the crystallization phenomena by DMA technique is not an often used method. But some earlier studies suggested that melt or intramolecular crystallization as a physical gelation behavior could be assessed with the viscoelastic measurements.[37–39] Furthermore, Chuang et al.[40] attempted to model isothermal cold-crystallization behavior of poly(trimethylene terephthalate) (PTT) by DMA measurements in three-point bending methods. As mentioned before, in cold-crystallization segmental dynamics of a semi-crystalline polymer is quite different from the transition from amorphous-melt to crystalline-solid. It is generally accepted that only the neighboring segments could associate together which is called intermolecular crystallization by gaining some energy above the glass transition temperature. The formation of fringed-micelle crystals in this case could be favored to the junction points in physical network structure.

As seen in Figure 9(a), the gap between the glassy and rubbery modulus of the film samples increases with the amount of organoclay. This could be originated from the effects of organic groups of organoclay on the segmental mobility and chain slipping under the condition of low amplitude strain. It can be concluded that more amount of organoclay which means more amount of organic ammonium compound in the system yielded higher loss in modulus. But, no correlation between the storage modulus at secondary plateau (at C) and sample composition by comparing the E' values is listed in Table IV. Dependence of loss factor (Tan δ) on the temperature is given in Figure 9(b). Peak temperature of Tan δ can be regarded as the glass-transition (T_g). Based on the DMA measurements, it was obtained that the T_g of I.30-1 was lower, whereas the I.30-3 and I.30-5 samples exhibited higher T_g values than PET. As distinct from the cold-crystallization endotherm monitored in the DSC runs, double peaks (or steps in E' curves) were observed for the cold-crystallization of film samples in DMA run. This behavior could be due to the effect of small amplitude of strain on the crystallization or annealing effect of relatively low heating rate (2°C min^{-1}) employed in DMA tests. Increase in crystallinity resulted in a physical enhancement in the structure and thus increase in the storage modulus during the test.

Table IV. Storage Modulus (E') Values of the Films at Different Regions Shown in Figure 9(a)

	E' (Pa)		
Samples	A	B	C
PET	1.1×10^9	4.7×10^7	2.4×10^8
I.30-1	1.5×10^9	4.0×10^7	1.7×10^8
I.30-3	1.9×10^9	3.1×10^7	1.9×10^8
I.30-5	2.6×10^9	1.5×10^7	1.5×10^8

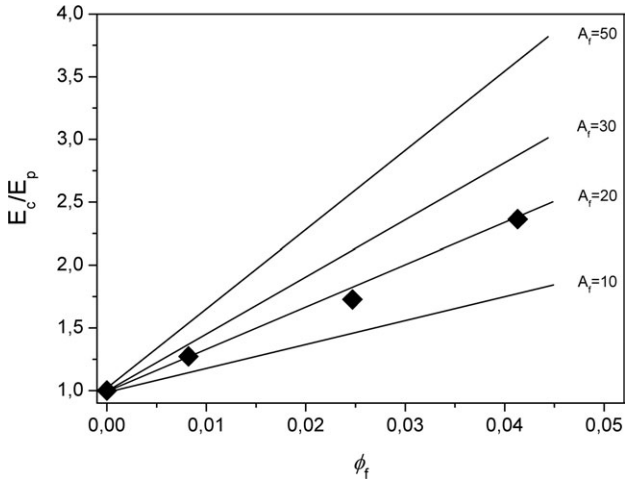

Figure 10. Halpin-Tsai model applied to DMA data of the samples for estimating the aspect ratio of clay layers.

The dependence of storage modulus on the volume fraction of filler can be quantified by micromechanical models. Thus, the aspect ratio of organoclay layer and/or stacks can be calculated. In this study, the Halpin-Tsai (H-T) model[41,42] which is a well known theory to predict stiffness of a composite material as a function of filler loading and aspect ratio was used to determine the aspect ratio of filler and estimate the microstructural features of samples. The Halpin-Tsai equation is expressed as:

$$\frac{E_c}{E_p} = \frac{1 + 2A_f \mu \phi_f}{1 - \mu \phi_f} \tag{5}$$

where E_c and E_p are the elastic modulus of composite and polymer, respectively. A_f refers to the aspect ratio of the filler. ϕ_f is the volume fraction of the filler and μ is the geometric factor which can be written as:

$$\mu = \frac{E_f/E_p - 1}{E_f/E_p + 2A_f} \tag{6}$$

where E_f is the elastic modulus of the filler. In this study, elastic modulus of a single clay layer and PET were taken as 176[43] and 1.1 GPa, respectively.

As shown in Figure 10, the H-T model predicts that the E_c increases almost linearly with the increasing of volume fraction of org-clay. Applying the data obtained from the DMA analysis of the samples, the H-T model predicts the A_f value about 20. This value is very consistent with the A_f value calculated from the SEM image analysis and gas permeability measurements.

CONCLUSION

In this study, thermal and physical properties of amorphous PET/organoclay nanocomposite films prepared with melt processing method were investigated, in detail. Highly transparent films, containing 1 and 3 wt % of organoclay, which exhibited superior physical performance and optical and aesthetical quality, were successfully obtained for possible using in packaging applications. Average aspect ratio (A_f) of clay stacks which is considered as one of the most important microstructural parameters was quantified with the SEM and DMA analysis and gas permeability measurements. These three methods yielded the same A_f value, 20, for the PET/organoclay nanocomposite films. It was also found that introducing organoclay affected differently cold- and melt-crystallization behavior of PET. Solid-state DMA tests of the films indicated that storage modulus in glassy region gradually improved with the amount of organoclay. It was also reported that cold-crystallization behavior of amorphous films can be precisely monitored with the low heating rate DMA measurements. Consequently, it is concluded that the microstructure of the PET/organoclay nanocomposite films, particularly I.30-3 and I.30-5, is formed uniformly dispersed intercalated clay stacks with the thickness of 20–30 nm and the width of 400–600 nm. Based on the intergallery distance (2.90 nm) obtained from the XRD analysis and the estimation of average A_f value from the quantifying physical properties of samples, these stacks probably consist of 5–8 clay layers (considering the individual layer thickness of 1 nm).

ACKNOWLEDGMENTS

The authors thank Mr. Selçuk Aksoy from Aksoy Plastik, Co. Inc., for his kind and valuable supports for the study by supplying materials and processing equipments used in the work.

REFERENCES

1. Ray, S.; Quek, S. Y.; Easteal, A. J.; Chen, X. D. *Int. J. Food Eng.* **2006**, *2*, 1.
2. Hu, Y. S.; Hiltner, A.; Baer, E. *J. Appl. Polym. Sci.* **2005**, *98*, 1629.
3. Hu, Y. S.; Prattipati, V.; Mehta, S.; Schiraldi, D. A.; Hiltner, A.; Baer, E. *Polymer* **2005**, *46*, 2685.
4. Polyakova, A.; Stepanov, E. V.; Sekelik, D.; Schiraldi, D. A.; Hiltner, A.; Baer, E. *J. Polym. Sci. Part B: Polym. Phys.* **2001**, *39*, 1911.
5. Aht-Ong, D.; Benjapornthavee, H. In the Proceeding Book of International Conference on Nanoscience and Nanotechnology, Melbourne, Australia, February 25–29, 2008; IEEE: New York, **2008**.
6. Ghasami, H.; Carrerau, P. J.; Kamal, M. R.; Uribe-Calderon, J. *Polym. Eng. Sci.* **2011**, *51*, 1178.
7. Ghasami, H.; Carrerau, P. J.; Kamal, M. R.; Chapleau, N. *Int. Polym. Process.* **2011**, *2*, 219.
8. Vidotti, S. E.; Chinellato, A. C.; Hu, G. H.; Pessan, L. A. *J. Polym. Sci. Part B: Polym. Phys.* **2007**, *45*, 3084.
9. Choi, W. J.; Kim, H. J.; Yoon, K. H.; Kwon, O. H.; Hwang, C. I. *J. Appl. Polym. Sci.* **2006**, *100*, 4875.
10. Lee, W. D.; Im, S. S.; Lim, H. M.; Kim, K. J. *Polymer* **2006**, *47*, 1364.
11. Vassiliou, A. A.; Chrissafis, K.; Bikiaris, D. N. *Thermochim. Acta* **2010**, *500*, 21.
12. Kim, D.; Lee, J. S.; Barry, C. M.; Mead, J. L. *Polym. Eng. Sci.* **2007**, *47*, 2049.
13. Bhimaraj, P.; Yang, H.; Siegel, R. W.; Schadler, L. S. *J. Appl. Polym. Sci.* **2007**, *106*, 4233.
14. Ge, C. H.; Ding, P.; Shi, L. Y.; Fu, J. F. *J. Polym. Sci. Part B: Polym. Phys.* **2009**, *47*, 655.
15. Lee, S. J.; Hahm, W. G.; Kikutani, T.; Kim, B. C. *Polym. Eng. Sci.* **2009**, *49*, 317.
16. Yesil, S.; Bayram, G. *Polym. Eng. Sci.* **2011**, *51*, 1286.
17. Zhang, H. B.; Zheng, W. G.; Yan, Q.; Yang, Y.; Wang, J. W.; Lu, Z. H.; Ji, G. Y.; Yu, Z. Z. *Polymer* **2010**, *51*, 1191.
18. Tzavalas, S.; Mouzakis, D. E.; Drakonakis, V.; Gregoriou, V. G. *J. Polym. Sci. Part B: Polym. Phys.* **2008**, *46*, 668.
19. Bandla, S.; Hanan, J. C. *J. Mater. Sci.* **2012**, *47*, 876.
20. Li, M.; Jeong, Y. G. *Compos. Part A: Appl. Sci. Manuf.* **2011**, *42*, 560.
21. Chung, J. W.; Son, S. B.; Chun, S. W.; Kang, T. J.; Kwak, S. Y. *J. Polym. Sci. Part B: Polym. Phys.* **2008**, *46*, 989.
22. Wang, Y.; Gao, J.; Ma, Y.; Agarwal, U. S. *Compos. Part B: Eng.* **2006**, *37*, 399.
23. Durmus, A.; Ercan, N.; Soyubol, G.; Deligoz, H.; Kasgoz, A. *Polym. Compos.* **2010**, *31*, 1056.
24. Calcagno, C. I. W.; Mariani, C. W.; Teixeira, S. R.; Mauler, R. S. *Polymer* **2007**, *48*, 966.
25. Phang, I. Y.; Pramoda, K. P.; Liu, T.; He, C. *Polym. Int.* **2004**, *53*, 1282.
26. Vyazovkin, S.; Stone, J.; Sbirrazzuoli, N. *J. Therm. Anal. Calorim.* **2005**, *80*, 177.
27. Chen, X. Q.; Xu, J. J.; Lu, H. B.; Yang, Y. L. *J. Polym. Sci. Part B: Polym. Phys.* **2006**, *44*, 2112.
28. Han, L.; Han, C.; Cao, W.; Wang, X.; Bian, J.; Dong, L. *Polym. Eng. Sci.* **2012**, *52*, 250.
29. Duan, B.; Wang, M.; Zhou, W. Y.; Cheung, W. L. *Polym. Eng. Sci.* **2011**, *51*, 1580.
30. Wu, D. F.; Wu, L.; Yu, G. C.; Xu, B.; Zhang, M. *Polym. Eng. Sci.* **2008**, *48*, 1057.
31. Oburoğlu, N.; Ercan, N.; Durmus, A.; Kasgoz, A. *J. Appl. Polym. Sci.* **2012**, *123*, 77.
32. Hu, G.; Zhao, C.; Zhang, S.; Yang, M.; Wang, Z. *Polymer* **2006**, *47*, 480.

33. Durmus, A.; Kasgoz, A.; Macosko, C. W. *Polymer* **2007**, *48*, 4492.
34. Sanli, S.; Durmus, A.; Ercan, N. *J. Mater. Sci.* **2012**, *47*, 3052.
35. Lange, J.; Wyser, Y. *Packag. Technol. Sci.* **2003**, *16*, 149.
36. Nielsen, L. E. *J. Macromol. Sci. Chem.* **1967**, *A1*, 929.
37. Shieh, Y. T.; Lin, Y. S. *J. Appl. Polym. Sci.* **2009**, *113*, 3345.
38. Kelarakis, A.; Mai, S. M.; Booth, C.; Ryan, A. J. *Polymer* **2005**, *46*, 2739.
39. Ma, C. G.; Chen, L.; Xiong, X. M.; Zhang, J. X.; Rong, M. Z.; Zhang, M. Q. *Macromolecules* **2004**, *37*, 8829.
40. Chuang, W. T.; Hong, P. D.; Shih, K. S. *Polymer* **2004**, *45*, 8583.
41. Halpin, J. C. *J. Comput. Mater.* **1969**, *3*, 732.
42. Halpin, J. C.; Kardos, J. L. *Polym. Eng. Sci.* **1976**, *16*, 344.
43. Chen, B.; Evans, J. R. G. *Scripta Mater.* **2006**, *54*, 1581.